3-D Thermal-Hydraulic Modeling an in-Cryostat Loss-of-Coolant Accident From a Superconducting Magnet

IEEE Access
Multidisciplinary : Rapid Review : Open Access Journal

Received 31 March 2026, accepted 7 May 2026, date of publication 13 May 2026, date of current version 18 May 2026.

Digital Object Identifier 10.1109/ACCESS.2026.3692921

RESEARCH ARTICLE

3-D Thermal-Hydraulic Modeling an in-Cryostat Loss-of-Coolant Accident From a Superconducting Magnet

MAURO SPRÓ, ANTONIO FROIO, AND ANDREA ZAPPATORE
NEMO Group, Dipartimento Energia, Politecnico di Torino 10129, Turin, Italy

Corresponding author: Mauro Spró (mauro.spro@polito.it)

This work was supported by European Union via the Euratom Research and Training Program within the Framework of the EUROfusion Consortium under Agreement 10105220–EUROfusion.

ABSTRACT Accidental transients in superconducting magnet systems for tokamak fusion reactors require thorough analysis, as they can jeopardize the integrity of critical, expensive, and often irreparable components like Toroidal Field (TF) coils. The in-cryostat Loss-of-Coolant Accident (LOCA) is particularly critical among these scenarios. This event is triggered by the release of pressurized Supercritical Helium (SHe), a phenomenon observed in experimental facilities, including ITER Central Solenoid Module (CSM) testing and JT-60SA commissioning. The SHe is discharged into the vacuum cryostat, forming an underexpanded supersonic jet; this rapid expansion results in a multiphase jet comprising supercritical, vapor, and liquid phases. Assessing potential magnet damage and developing diagnostics requires detailed knowledge of the 3D evolution of pressure and temperature distributions. Therefore, a 3D Computational Fluid Dynamics (CFD) model is essential for capturing the complex spatial and temporal dynamics of cryostat pressurization and jet propagation. In this work, a 3D transient analysis of the in-cryostat LOCA is performed, using a simplified ITER CSM geometry. The model simulates the SHe jet propagation from the moment of rupture for several minutes, allowing sufficient time for the module to heat-up. The physical models, especially the multiphase model, are validated against a 2D benchmark problem before application to the 3D scenario. In addition, an Adaptive Mesh Refinement algorithm dynamically tracks the expected shock fronts. Particular attention is paid to the temperature distribution in the CSM, with its evolution monitored from the onset of the accident to the end of the transient.

INDEX TERMS CFD, LOCA, multiphase flow, nuclear fusion, superconducting magnets, supercritical helium, underexpanded jet.

I. INTRODUCTION

The numerical analysis of accidental transients in fusion reactors is of fundamental importance for the design and operation of tokamaks, especially with regard to accidents that can jeopardize entire components and therefore cannot be tested in full-scale experimental facilities to identify potential damage and mitigation strategies.

A fusion reactor can experience different types of Loss-Of-Coolant Accidents (LOCAs), among which the in-cryostat LOCA affecting the superconducting magnet system is one of the most critical. Although this event shares some phenomenological similarities with other LOCA scenarios, such as in-box LOCAs in the breeding blanket [1], [2] and in-vessel LOCAs, which have been investigated through 0D system-level codes and, more recently, 3D CFD simulations for both helium [3] and water [4], the in-cryostat LOCA remains comparatively less explored. This accident is typically initiated by a breach in a cryogenic cooling line or in a component located inside the cryostat. The sudden release of cold helium into the cryostat volume triggers a rapid sequence of coupled thermal–hydraulic phenomena: the discharged helium warms up and expands, generating a fast pressurization of the cryostat; part of the flow can

The associate editor coordinating the review of this manuscript and approving it for publication was Simone Minucci.

impinge on nearby structures, enhancing heat transfer and potentially inducing local thermal shocks. As the pressure rise propagates, relief and venting systems may activate, but their performance strongly depends on the transient evolution and on the two-phase flow conditions that develop as the helium continues to warm and vaporize. If not mitigated, an in-cryostat LOCA can lead to several detrimental consequences. The pressure excursion can challenge the structural integrity of the cryostat and its penetrations; the sudden temperature increase around superconducting coils can trigger a quench, with large thermal gradients that may damage windings or supports. The lack of validated modeling approaches for this scenario underscores the need for dedicated numerical tools capable of capturing the fast, strongly coupled fluid–structure interactions involved.

The main objective of this work is to develop a general model for the release of pressurized fluids into vacuum environments, focusing on the accidental transient that occurred at an experimental facility in San Diego, where the ITER Central Solenoid Modules (CSMs) are tested prior to shipment to the actual construction site [5]. Recent literature has investigated helium LOCAs focusing on real gas effects in 2D short-term transients (e.g., [6]) or steady-state natural convection in DEMO-like cryostats (e.g., [7]). However, these approaches present significant physical and temporal limitations. Specifically, while [6] addresses real gas behavior, it neglects helium phase change during the expansion. By ignoring the energy partition and density changes associated with phase transition, such models potentially overestimate the jet momentum. Furthermore, these existing studies either limit the analysis to the first second of the accident [6] or neglect the initial supersonic jet dynamics entirely, relying on simplified 1D heat conduction models for the cryostat temperature evolution [8]. The present work addresses these gaps by introducing a 3D multi-time scale framework capable of resolving the full transient evolution, explicitly accounting for phase change transition, from the initial vacuum expansion to the long-term thermal diffusion within the superconducting modules. The paper is organized as follows: Section II describes the assumed scenario and computational domain, including the relevant simplifications introduced; Section III presents the simulation setup, including boundary and initial conditions, adopted models and solvers, mesh adaptation strategy, and multi-time scale solution approach; Section IV presents and discusses the results. Finally, Section V reports the conclusions and future perspectives.

II. SCENARIO AND GEOMETRY DESCRIPTION

The scenario considered for the analysis is a LOCA inside the cryostat of the San Diego testing facility (see Fig. 1). The accident occurred during a 15 kA AC loss test (i.e., a fast discharge to induce and measure AC losses in the coil) on CSM3, when an abnormal event took place immediately after the fast discharge was triggered. This led to a rapid pressure increase, activation of pressure relief valves, and confirmation of a helium breach. Post-event inspections identified arc faults and damage to the coaxial joints and helium containment, although the investigations could not determine whether the arc fault or the helium breach occurred first [9]. The helium coolant (reference thermodynamic conditions: 6 bar, 4.5 K) was then rapidly released inside the cryostat in the form of a two-phase underexpanded jet.

FIGURE 1. The San Diego testing facility [10].

The ITER Central Solenoid (CS) is composed of six modules (see Fig. 2a). Each module consists of individual winding layers, referred to as pancakes. These are arranged as a stack of six hexa pancakes and one central quad pancake, providing a total of 40 pancakes in the axial direction and 14 turns in the radial direction, as shown in Fig. 2b. The winding pack is cooled by supercritical helium, with the helium inlets located at the inner radius of the module and the outlets at the outer radius. Each pancake is made of multi-material Cable-In-Conduit-Conductors (CICCs), consisting of a central stainless-steel spiral, Nb_3Sn superconducting strands bundled with copper stabilizer, a stainless-steel jacket, and glass epoxy resin electrical insulation. An example of CICC is shown in Fig. 2c.

The break is assumed to be located at the 1st pancake, thus allowing the exploitation of radial symmetry. Consequently, the computational domain consists of half of the module and half of the cryostat. Fig. 3 shows the computational domain properly labeled with the different components, as well as a zoomed-in view of the inlet section area. The rupture is assumed to be circular, with a radius of 1 cm.

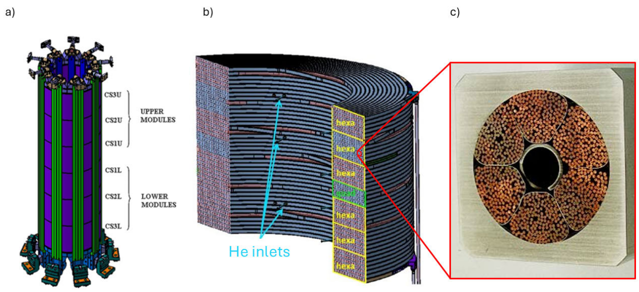

FIGURE 2. a) ITER Central Solenoid, b) Single CSM details [11], c) Single CICC details [12] (the insulation is not shown here).

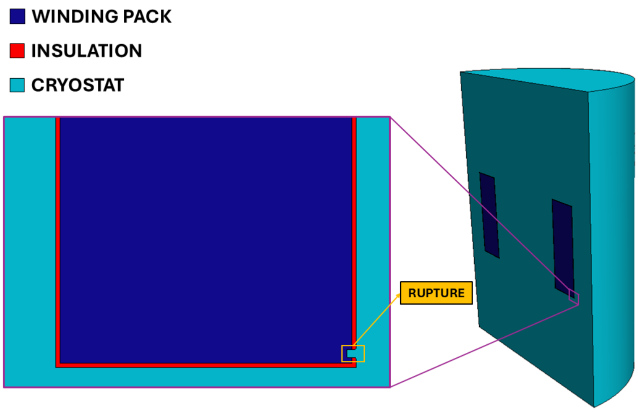

FIGURE 3. Adopted computational domain.

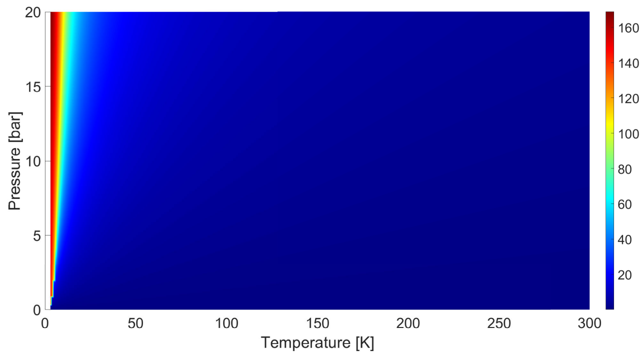

FIGURE 4. Computed helium density in kg/m^3 as a function of pressure and temperature.

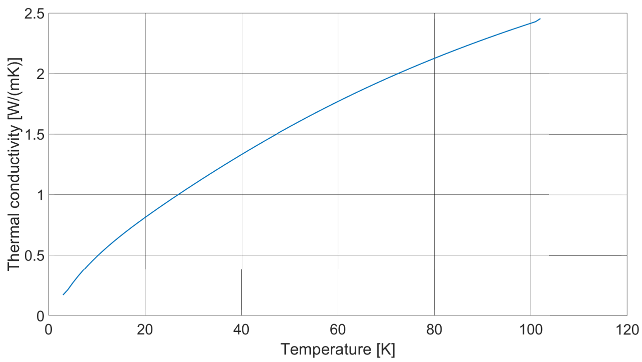

FIGURE 5. Module thermal conductivity as a function of temperature.

III. SIMULATION SETUP

This section describes the setup adopted for the CFD model. The software used for the simulation is STAR-CCM+ v16.04 [13].

A. THERMOPHYSICAL PROPERTIES

1) SHE PROPERTIES

The thermodynamic properties (density, specific enthalpy, specific entropy, specific heat, speed of sound, saturation pressure, and saturation temperature) and the transport properties (dynamic viscosity and thermal conductivity) required for the calculation were computed in MATLAB using the free CoolProp library [14]. Each property was evaluated over a wide pressure and temperature range (0.01 bar-20 bar and 3 K-300 K) and then tabulated in a suitable format for inclusion in STAR-CCM+. For illustrative purposes, the resulting density is shown in Fig. 4.

2) INSULATION AND CSM PROPERTIES

For the solid components, the required tabulated properties included density, specific heat, and thermal conductivity. Density was assumed constant for all materials. Specific heat and thermal conductivity of the insulation were computed directly by means of polynomial functions [15], [16]. The specific heat of the module was instead calculated as a mass-weighted average of the specific heat values of its constituent materials [17], [18], [19]. The thermal conductivity of the module, on the other hand, was evaluated using a different approach. A 2D, heat diffusion simulation of half of a multi-material CICC was performed 100 times. The conductor initial temperature, as well as its left and right boundary temperatures, were increased by 1 K in each simulation (e.g., during the 1$^{\text{st}}$ run: $T_0 = 3\,\text{K}$, $T_{\text{left}} = 2\,\text{K}$, and $T_{\text{right}} = 4\,\text{K}$) and the volume-averaged conductivity was then extracted. This procedure made it possible to obtain a uniform thermal conductivity for the entire module over a temperature range from 3 K to 102 K. Fig. 5 shows the obtained temperature-dependent thermal conductivity.

B. BOUNDARY AND INITIAL CONDITIONS

1) BOUNDARY CONDITIONS

The selected boundary conditions are shown in Fig. 6: The "Stagnation inlet" is the boundary condition used by the software to impose total pressure and temperature values, as well as void fraction (for multiphase problems), at an inlet [20].

This boundary condition requires both the static pressure p_s (assumed to be constant and equal to 6 bar) and the total pressure p_t to be prescribed at the inlet. The total pressure can be calculated using the following equation:

$$\frac{p_t}{p_s} = \left(1 + \frac{\gamma - 1}{2}(\text{Ma})^2\right)^{\frac{\gamma}{\gamma-1}} \qquad (1)$$

where γ is the ratio of specific heats of the gas and Ma is the Mach number, which represents the ratio between the fluid velocity at the boundary and the speed of sound in the medium. Since Ma is a simulation output, it is recalculated at every solver iteration on the inlet surface and substituted into (1).

The total temperature T_t is also imposed, following the equation:

$$\frac{T_t}{T_s} = 1 + \frac{\gamma - 1}{2}(\mathrm{Ma})^2 \tag{2}$$

where T_s is the static temperature (4.5 K) and Ma is computed at each iteration as discussed above. The choice of a constant stagnation pressure (6 bar) and temperature (4.5 K) at the inlet is based on the large inventory of supercritical helium in the cooling circuit compared to the amount discharged during the first 150 s of the transient. This simplification allows focusing on the cryostat's thermal-hydraulic response under a conservative "steady-leak" assumption. The temperature on the external walls is fixed at 300 K.

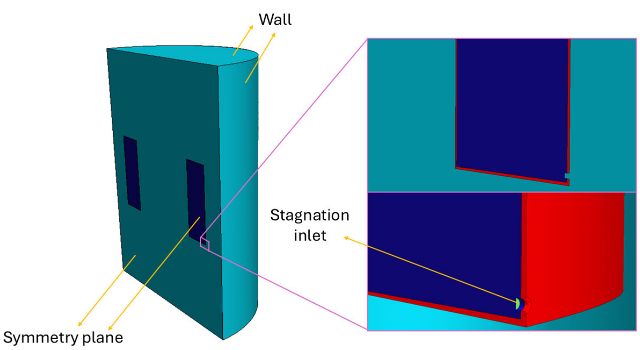

FIGURE 6. Boundary conditions.

2) INITIAL CONDITIONS

The cryostat is modeled as being filled with helium vapor at a static pressure of 0.1 bar for computational purposes. This particular value of static pressure is chosen to meet the continuum assumption, specifically to achieve a low Knudsen number (Kn $\sim 1.7 \times 10^{-6}$), defined as:

$$\mathrm{Kn} = \frac{\lambda}{L} = \frac{k_B T}{\sqrt{2}\pi\sigma^2 pL} \tag{3}$$

with:

- λ: molecular mean free path
- L: characteristic length (in this case the distance between the inlet and the wall in front of it)
- k_B: Boltzmann constant
- T: temperature of the system
- σ: particle diameter
- p: pressure of the system

As noted in [3], [4], and [6] this assumption can be considered analogous to assessing the transient behavior after the initial moments, when the continuum hypothesis becomes valid, thus the choice of an initial background pressure of 0.1 bar represents a modeling trade-off. While it ensures the validity of the Navier-Stokes equations throughout the simulation, it simplifies the physics of the very first expansion into high vacuum. Regarding the temperature, the initial distribution was computed through a steady-state thermal simulation and mapped onto the LOCA model. This simulation adopted the same domain shown in Fig. 3, but without the rupture. For the calculation of helium thermodynamic properties, a pressure of 0.1 bar was considered, and wall temperatures of 300 K and 4.5 K were imposed for the cryostat and for the module, respectively. Fig. 7 shows the resulting initial temperature distribution on the symmetry plane.

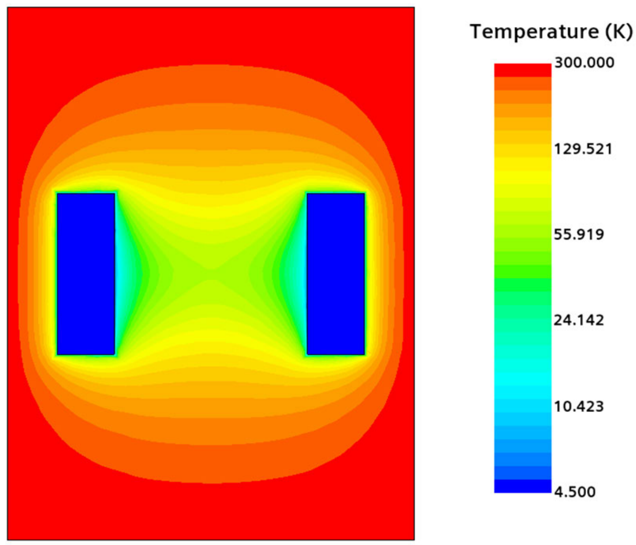

FIGURE 7. Initial temperature distribution.

C. MODELS AND SOLVERS

1) MODELS

The analysis of this problem required a multiphase approach to account for the phase change occurring when the SHe expands and becomes a liquid-vapor mixture. The first step involved selecting an appropriate model among those available in the software to solve the Equation of State (EOS) and handle phase interactions. The most suitable multiphase model is, in principle, the Volume of Fluid (VOF), as it allows the activation of the Homogeneous Relaxation Model (HRM) for phase interaction. The HRM relies on a finite-rate formulation for the evolution of the vapor mass fraction, making it particularly appropriate for phase-change processes under thermal non-equilibrium conditions (see [21] for a detailed comparison with other simpler models). However, the VOF model cannot be employed together with a coupled pressure-velocity solution scheme, which is essential in this work due to the underlying physical mechanisms and the relatively high Mach number involved. Therefore, to enable the use of a coupled scheme, and considering the large computational domain ($\sim 88\,\mathrm{m}^3$, corresponding to $\frac{1}{2}$ of the total cryostat volume), a simplified

Multiphase Mixture implementation was selected: the "Two-Phase Thermodynamic Equilibrium (2PTE) Model." In this model, the computational effort is reduced by assuming the suspension to be a homogeneous single-phase system. The distribution of static enthalpy, together with the assumption of thermodynamic equilibrium, is used to determine the distribution of phases [20]. The effectiveness of this model in capturing the phase change under consideration has been validated against results from the literature, as detailed in the Appendix A. Regarding the Navier-Stokes equations, as mentioned above, a coupled approach is preferred for compressible flows; therefore, the "Coupled Flow" and "Coupled Energy" models were selected. The local Reynolds number, calculated using the equation:

$$\mathrm{Re} = \frac{\rho v D}{\mu} \tag{4}$$

where ρ is the average fluid density, v is the average velocity, D is the rupture diameter, and μ is the fluid dynamic viscosity, exceeds 2.3×10^6 throughout the jet region during the expansion process, indicating a fully turbulent flow regime. The SST $k - \omega$ turbulence model was selected to resolve the flow physics of the underexpanded helium jet. This model is particularly effective in handling the adverse pressure gradients and shock-boundary layer interactions that characterize supersonic expansions into low-pressure environments [22], [23], [24], [25]. Furthermore, for large-scale 3D domains ($88\,\mathrm{m}^3$ in the current work) where the computational cost of scale-resolving simulations like LES is prohibitive, the RANS-based SST $k - \omega$ remains the industry standard for high-Reynolds number flows ($\mathrm{Re} > 2.3 \times 10^6$ in this study) involving complex shock structures [26]. The reliability of this choice is also supported by recent similar investigations on helium releases in fusion environments [3], [6]. To further quantify the sensitivity of the results to the turbulence closure, a comparative study was performed between the baseline SST $k - \omega$ and the Realizable $k - \varepsilon$ (Two-Layer formulation) for the initial 4 ms.The deviation was assessed via the Root Mean Square (RMS) of the volume-averaged relative error, computed as:

$$\mathrm{RMS} = \sqrt{\frac{1}{V} \int \left(\frac{\phi_{k-\varepsilon} - \phi_{k-\omega}}{\phi_{k-\omega}} \right)^2 \mathrm{d}V} \tag{5}$$

where ϕ represent the quantity of interest (pressure, velocity or temperature). The resulting RMS deviations are: $\mathrm{RMS_p} = 2.4\%$, $\mathrm{RMS_v} = 11.1\%$, and $\mathrm{RMS_T} = 24.5\%$. The discrepancies are strictly confined to the high-gradient regions of the jet's shear layer and the stagnation zone, whereas the core of the flow remains largely consistent. Overall, the impact of the turbulence model selection on the global flow evolution is limited, confirming the established suitability of the SST $k - \omega$ model for the physics of the problem investigated in this work. Furthermore, since Adaptive Mesh Refinement (AMR) is also employed (see Section III-D), the "Solution Interpolation" model is enabled to allow the interpolation of the solution from the old mesh to the new one whenever the mesh is adapted.

2) SOLVERS

Given the complexity of the problem, the solver settings must be carefully adjusted. The selected solvers are listed below.

1) Implicit unsteady
   a) A maximum time step of 1 µs was initially imposed and then progressively increased to 4 µs during the jet expansion phase. Once this critical stage passed, the maximum time step was raised to 1 ms.
2) Adaptive time step
   a) Due to the significant difference between upstream and downstream pressure, the startup phase of the transient is the most critical period. A strategy analogous to that employed in [4] is used to automatically adjust the time step based on the Courant-Friedrichs-Lewy (CFL) number, i.e., the CFL associated with the actual flow-field time integration. In this case, the target average and maximum CFL values were set to 1 and 10, respectively, whereas the Time-Step Change Factor was set to 1.2 (i.e., the time step increases by a factor 1.2 whenever the CFL condition is met). Throughout the jet expansion phase, the average time step was approximately 3 µs; in the subsequent phase, it increased to 0.6 ms.
3) Coupled implicit
   a) An automatic solver-CFL approach was used, with values ranging from 0.01 to 0.1 and a constant relaxation factor of 0.1. Unlike the physical CFL used for the adaptive time-step strategy, this solver-CFL is an internal pseudo-CFL that governs the stability and convergence behavior of the coupled implicit iterations. It controls the amount of information propagated during each nonlinear iteration and therefore acts as a numerical stabilization parameter rather than a constraint on the physical time integration.
   b) AMG linear solver
      i. V-type cycle (max cycles = 30)
      ii. Convergence tolerance = 0.1
      iii. Acceleration method: Bi-Conjugate Gradient Stabilized (BiCGStab)

D. ADAPTIVE MESH REFINEMENT

Given the need to accurately capture shock-front propagation, an adaptive mesh is essential for optimizing mesh generation and tracking these fronts. This is achieved using an adaptation strategy similar to that employed in [4]. In this case, a polyhedral mesher was selected among the different volume meshers available in STAR-CCM+. The choice was driven by the efficiency of this type of mesh, which is relatively easy to build and requires approximately five times fewer cells than a tetrahedral mesh for a given starting surface [20]. The Adaptive Mesh Refinement (AMR) settings were implemented as follows. A "User-Defined mesh adaption" was implemented to dynamically capture the complex shock structures and slipstreams. The refinement is driven by a customized field function ϕ, defined as the local Mach number variation:

$$\phi = \Delta \text{Ma} = ||\nabla \text{Ma}||\ \delta \quad (6)$$

where δ represents the local cell size. This formulation ensures that the mesh density is directly coupled to the flow gradients. To guarantee high resolution in the jet core while maintaining computational efficiency, two critical constraints were defined:

- **Minimum Cell Size:** The refinement process is bounded by a target minimum cell size (δ_{min}) of 0.8 mm. This threshold was selected through a gradient-sensitivity analysis to ensure that the primary shock features were numerically resolved without excessive computational overhead.
- **Refinement Levels:** The maximum number of refinement levels was set to a high threshold (up to 10 levels). By effectively leaving this parameter unbounded, the discretization process is governed exclusively by the physical gradients and the minimum cell size limit, preventing any artificial effect of the mesh evolution in regions of extreme flow variations.

The resulting refinement algorithm follows a three-step logic based on the local evaluation of ϕ within a specified range (set to [0.1, 0.3] in this study):

- $\phi > 0.3$: The cell is **refined** to better resolve the local gradient.
- $0.1 \leq \phi \leq 0.3$: The current resolution is **kept** as the gradient is sufficiently captured.
- $\phi < 0.1$: The cell is **coarsened** to optimize computational resources in low-gradient regions.

In addition, because the insulation is a very narrow volume, the "Thin Mesher" was used in combination with the polyhedral mesher. This type of volume mesher allows significant cell savings by generating a prismatic-type volume mesh for thin regions, whereas thicker or bulk portions of the same geometry are meshed using the core volume mesher [20]. The resulting mesh (at $t = 2.0$ ms and $t = 10.5$ ms) is shown in Fig. 8, highlighting both the Thin Mesher and the AMR. To ensure the numerical robustness of the proposed AMR strategy, a grid independence analysis was conducted. The study focused on the first 4.0 ms of the transient, providing sufficient time for the underexpanded jet to initiate and the Mach disk to reach its early-stage development. This timeframe is particularly critical as it involves the steepest pressure and velocity gradients, posing the most significant challenge for the refinement algorithm. By varying the minimum cell size, the stability of the shock front capturing was verified. Further details regarding the mesh sensitivity study and the convergence of key parameters are provided in Appendix B.

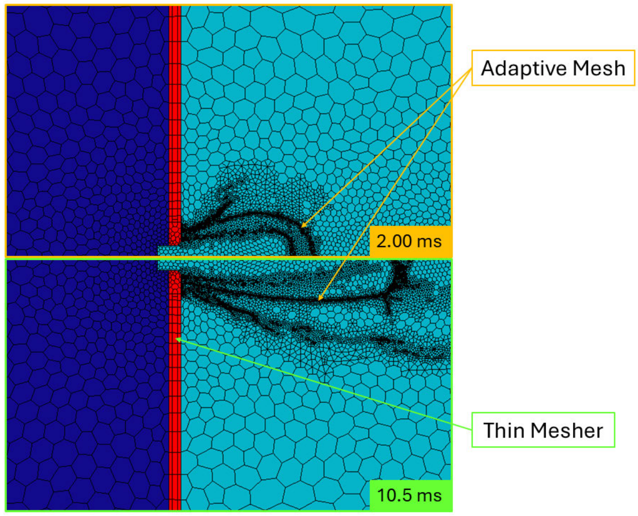

FIGURE 8. Mesh detail on the frontal symmetry plane at 2.0 ms **and** 10.5 ms **(The color legend is analogous to that of Fig. 3).**

E. MULTI-TIME SCALE SOLUTION STRATEGY

The accidental SHe release involves a challenging multi-spacescales and multi-timescales transient, characterized initially by a rapidly evolving underexpanded jet (during which the helium goes from the supercritical phase to the vapor phase) and, subsequently, by a much slower large-scale dispersion of helium vapor inside the cryostat. To efficiently handle this strong separation of temporal and spatial scales, the simulation was divided into three main phases. Each phase employs a domain manipulation strategy inspired by SBAM-like approaches [27], reducing computational cost while preserving physical accuracy.

1) **Phase 1 - Jet expansion and Mach disk formation** The simulation begins with the full computational domain. During the first few milliseconds, the jet undergoes a supersonic expansion, forming a spherical shock front and a Mach disk. This region requires the highest refinement due to steep gradients and shock fronts. Phase 1 ends when the Mach disk stops expanding both axially and radially, indicating that the jet structure has stabilized.
2) **Phase 2 - Domain reduction and long-term evolution** Once the Mach disk becomes quasi-stationary, it is removed from the simulation domain. The quasi-stationarity of the jet is checked by monitoring the pressure, velocity, and temperature profiles along horizontal and vertical line probes on the disk, and confirming that they remain unchanged for several seconds. As shown in Fig. 9, a new computational domain is then generated, with the inlet relocated to the surface created by the domain cut. The flow solution in the retained portion of the domain is exported and mapped onto the new mesh. This operation decreases the number of cells by more than a factor of two (from ∼ 5.5M to ∼ 2M), significantly accelerating

computations and allowing for a larger time step during the slow cryostat-filling phase, as previously discussed in Section III-C2. The jet then continues to evolve under gravity and buoyancy until t = 150 s.

3) **Phase 3 - Domain reconstruction and valve opening** In the real accidental event, a safety valve opened when the helium pressure in the internal cryogenic circuit reached 16 bar, diverting the SHe flow to the storage system and stopping the discharge into the cryostat. In this work, this moment was assumed to occur after approximately two and a half minutes ($t \approx 150$ s). To reproduce this condition, the previously removed portion of the domain is reconstructed, thus restoring the configuration of Phase 1 shown in the upper half of Fig 9. The solution is mapped onto the full geometry, and the inlet boundary is converted into a wall, effectively preventing further helium injection. After this operation, the jet rapidly dissipates. As gradients weaken, AMR progressively coarsens the mesh, reducing the domain to roughly 3×10^5 active cells (almost 20 times fewer than during the initial jet expansion), highlighting the benefit of employing an AMR solver as opposed to a uniformly refined static mesh.

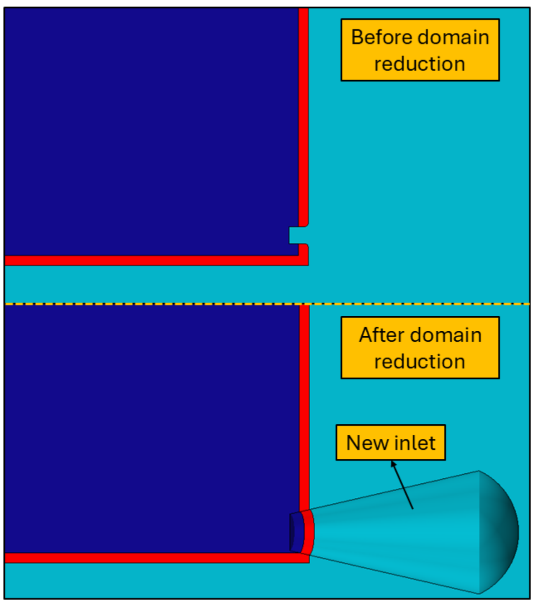

FIGURE 9. Simulation domain before and after the reduction.

IV. RESULTS

This section presents and discusses the main results of the 3D model.

A. FLOW FIELD

1) **Phase 1** The early evolution of the SHe jet is reported in Fig. 10. Immediately after the rupture, the flow expands supersonically into the cryostat, forming a spherical shock front with a peak Mach number of $Ma_{MAX} = 2.1$ (Fig. 10a). At approximately 10.5 ms, two slipstreams start detaching from the jet core, as expected in underexpanded jets [28], [29]. As the jet continues to expand, the Mach disk gradually grows until it reaches a quasi-stationary size and position (Fig. 10c–e). At this point, corresponding to the end of Phase 1, the domain reduction strategy is applied (Fig. 10f), as detailed in Section III-E.

2) **Phase 2** The second phase of the transient is shown in Fig. 11a–b. Following the domain reduction, the jet continues to propagate both upward and downward, with gravity also driving the downward motion. During the long-term dispersion, the dominant mechanism shifts from momentum-driven expansion to buoyancy-driven circulation. The primary source of thermal load comes from the localized impingement on the CSM bottom, with peak heat fluxes observed in the area closest to the rupture, highlighting the necessity of a 3D model over 0D/1D safety assessments. This phase covers the long-time behavior up to 150 s, during which the cryostat gradually fills with cold helium. The AMR solver adapts the mesh dynamically, maintaining refinement only around the evolving jet structures while coarsening regions where gradients become negligible, thus ensuring computational efficiency.

3) **Phase 3** The effect of the domain reconstruction is visible in Fig. 11c–f: the jet dissipates rapidly once the mass flow is interrupted.

B. TEMPERATURE FIELD

The temperature field at different time instants is shown in Figs. 12,13. It can be observed that, after a few milliseconds (Fig. 12a), the temperature field still reflects, to some extent, the initial distribution. Moreover, consistently with the expansion process, the jet core rapidly cools down, reaching temperatures as low as 3 K. It should be noted, however, that as a consequence of the initial cryostat pressure assumption (see III-B2 above) results within the first few milliseconds (e.g. Fig. 12a) should be considered as an engineering approximation of the jet development rather than a strict representation of the vacuum-to-continuum transition. When the Mach disk becomes steady (i.e., after approximately 10.0 s), the average temperature inside the cryostat approaches a constant value, whereas the CSM temperature continues to rise, as can be seen in Fig. 13, where the thermal boundary layer inside the module becomes progressively thicker. When the transient ends, the average cryostat temperature is around 110 K, whereas the average module temperature reaches approximately 6.3 K.

To assess whether the heating of the module poses a risk to the magnet system's safety, the heat fluxes on the internal and external walls were monitored throughout the entire simulation at several probe points, positioned to match the locations of the temperature sensors embedded in the double-pancake structure (see Fig. 14). These fluxes

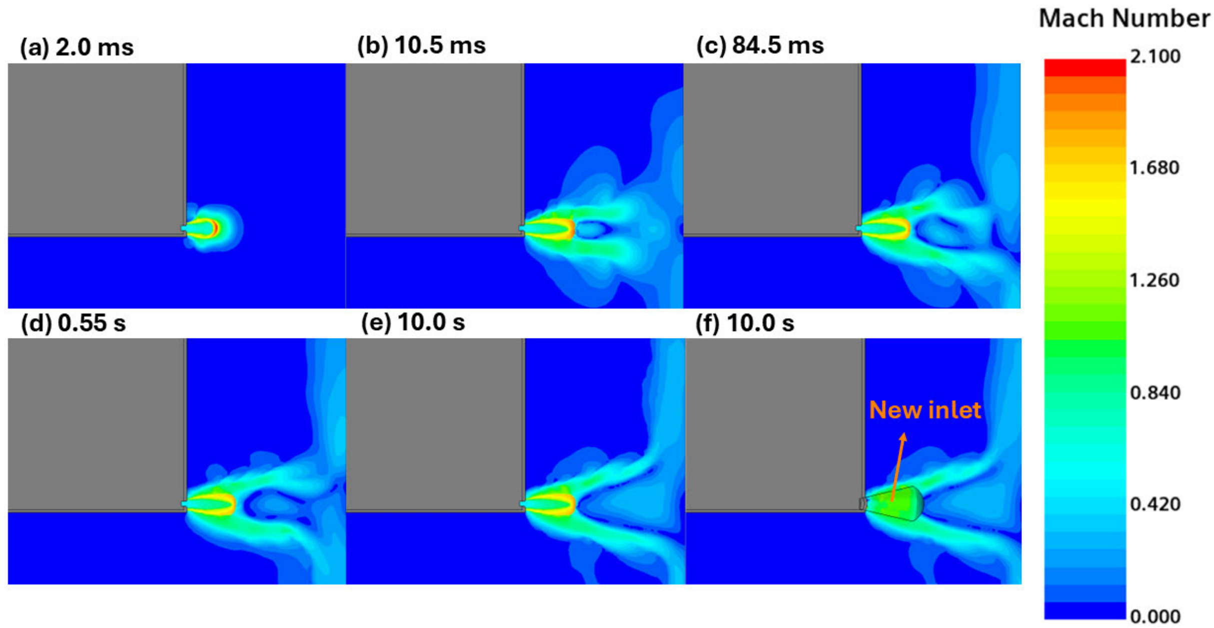

FIGURE 10. Mach number distribution on the symmetry plane at (a) t = 2.0 ms, (b) t = 10.5 ms, (c) t = 84.5 ms, (d) t = 0.55 s, (e) t = 10.0 s before the domain reduction, and (f) t = 10.0 s after the domain reduction.

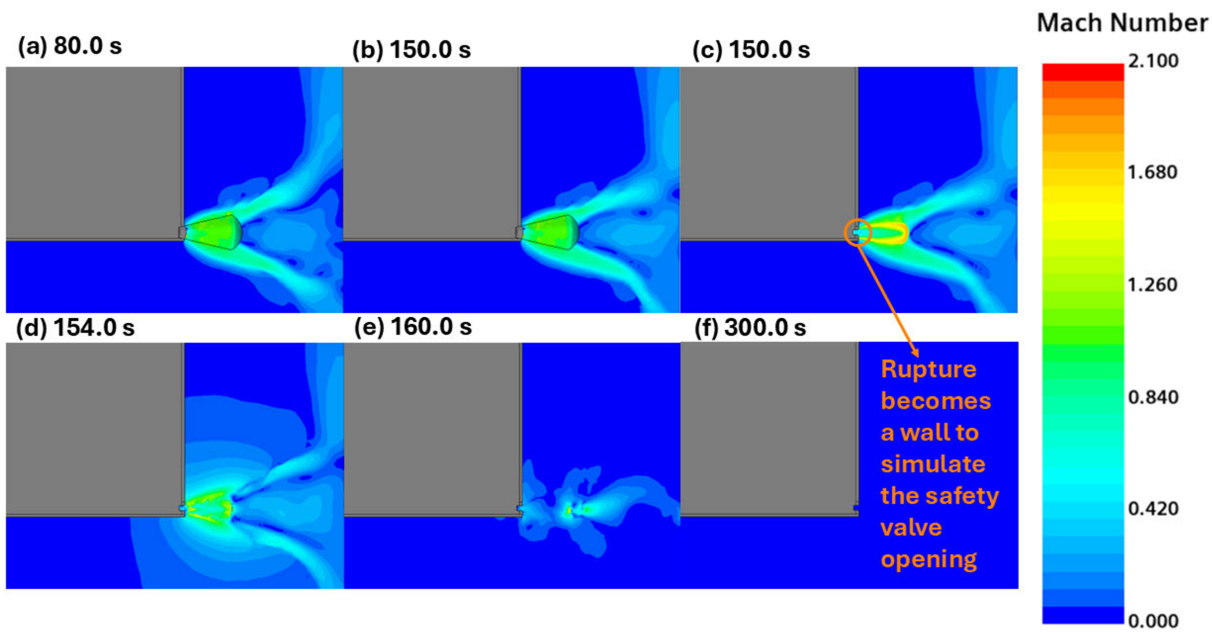

FIGURE 11. Mach number distribution on the symmetry plane at (a) t = 80.0 s, (b) t = 150.0 s before the domain reconstruction, (c) t = 150.0 s after the domain reconstruction, (d) t = 154.0 s, (e) t = 160.0 s, and (f) t = 300.0 s.

can be then exported and tabulated in a suitable format for inclusion in the Cryogenic Circuit, Conductor, and Coil (4C) code [30], which enables the thermal-hydraulic analysis of the entire superconducting magnet system. The heat flux evolution on the CSM external wall reveals a peak value of nearly $\sim$550 W m^{-2} at the sensors closest to the jet impingement zone. This intensity is sufficient to drive the average module temperature from 4.5 K to 6.3 K within a few minutes. However, the thermal diffusion within the insulation (modeled with the 'Thin Mesher') acts as a significant buffer, as shown by the thermal boundary layer thickness in Fig. 13, which prevents an immediate and catastrophic global quench during the first seconds of the SHe release. The thermal boundary layer in the CSM (Fig. 13) increases from $\sim$0.02 m at 10 s to $\sim$0.10 m at 300 s, providing a quantitative measure of the insulation's effectiveness in delaying the quench of the superconducting strands.

C. PRESSURE EVOLUTION

The pressure behavior was analyzed throughout the transient as the shock wave propagated within the cryostat. The

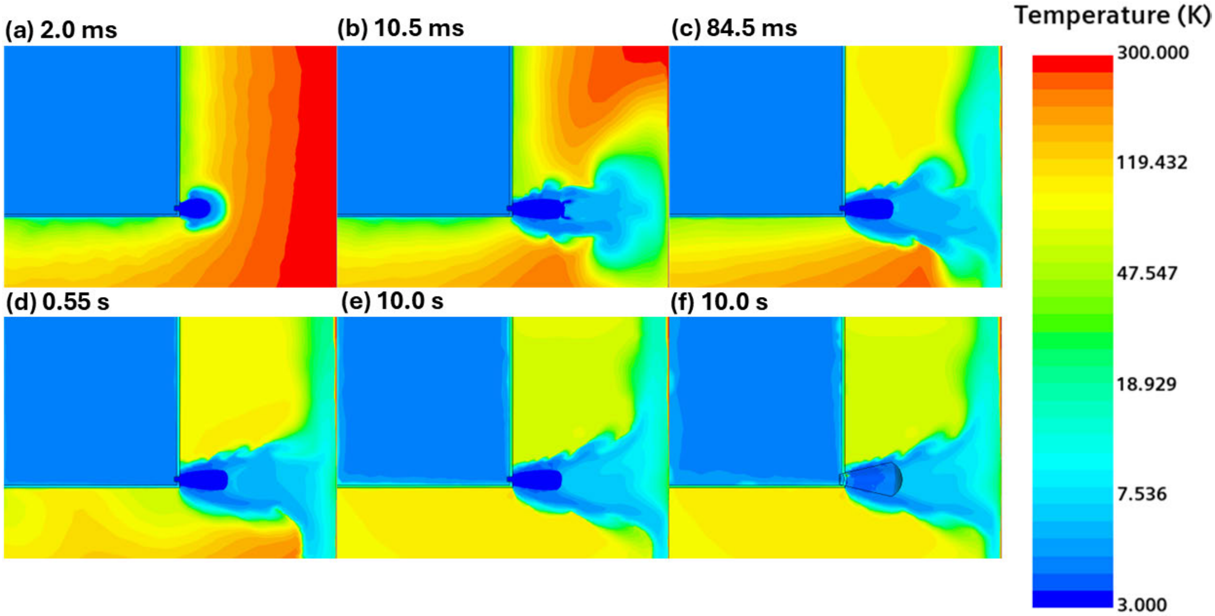

FIGURE 12. Temperature distribution on the symmetry plane at (a) t = 2.0 ms, (b) t = 10.5 ms, (c) t = 84.5 ms, (d) t = 0.55 s, (e) t = 10.0 s before the domain reduction, and (f) t = 10.0 s after the domain reduction.

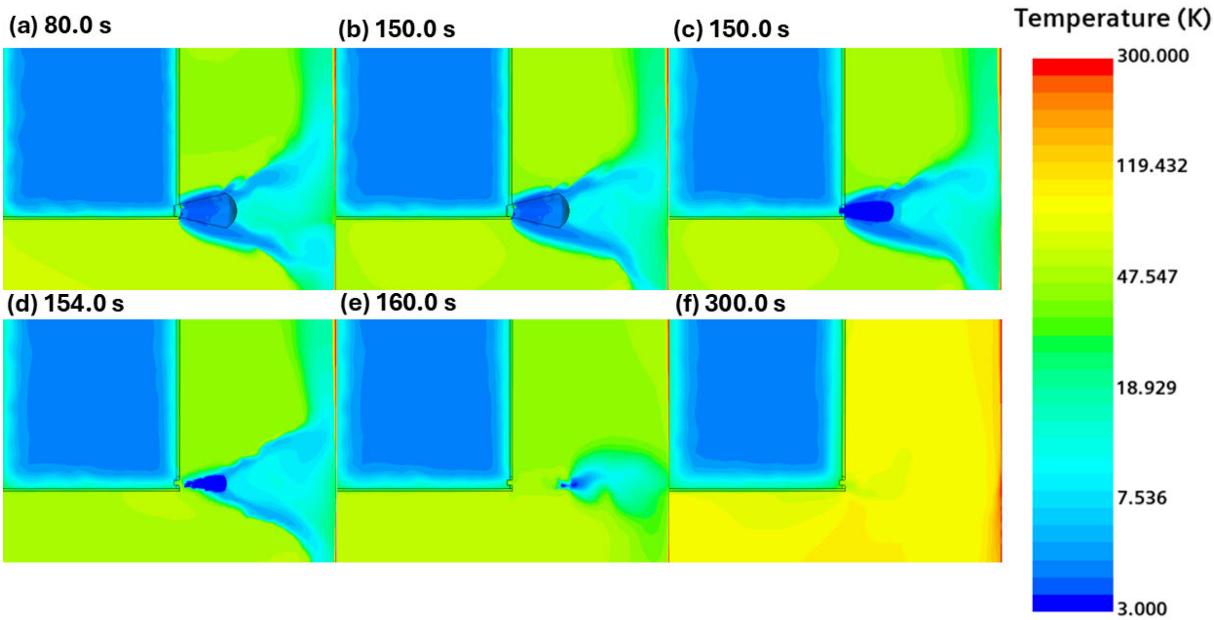

FIGURE 13. Temperature distribution on the symmetry plane at (a) t = 80.0 s, (b) t = 150.0 s before the domain reconstruction, (c) t = 150.0 s after the domain reconstruction, (d) t = 154.0 s, (e) t = 160.0 s, and (f) t = 300.0 s.

primary objective was to monitor the evolution of the average pressure inside the cryostat, in order to determine whether excessive pressurization might occur during the transient. The results show that the transient led to a slight pressurization of the cryostat, as illustrated in Fig. 15, which does not pose any concern for the operational safety of the system.

A secondary objective was to assess whether the pressure peak resulting from the jet impact on the wall in front of the rupture could compromise the structural integrity of the cryostat. As shown in Fig. 16, the pressure increases only from 0.10 bar to approximately 0.13 bar, indicating no significant risk to structural components.

The pressure distribution in the underexpanded jet, at $t = 10.5$ ms, is also shown in Fig. 17. As can be seen, the rapid expansion of the SHe results in a marked pressure drop, with the minimum value (0.014 bar) occurring at the location where the fluid reaches its maximum velocity and lowest temperature.

A summary table (Table 1) with the values of the most important safety-related parameters is reported below.

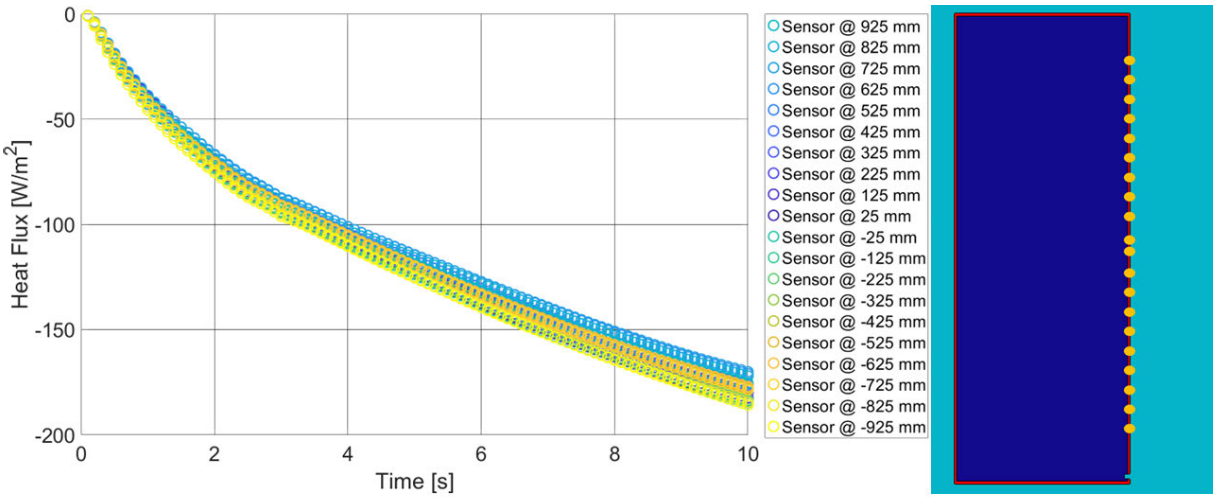

FIGURE 14. Heat fluxes evolution on the module external wall during the 1st phase (left); location of the sensors on the module external wall (right).

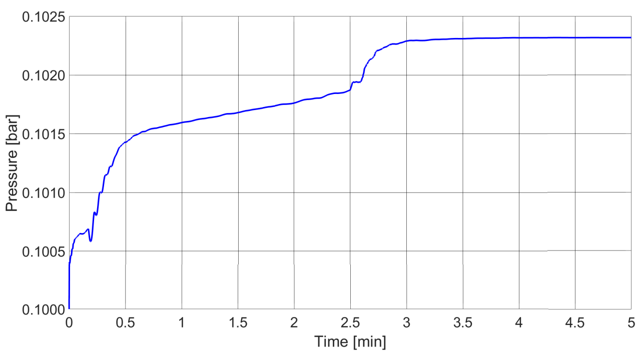

FIGURE 15. Average cryostat pressure evolution.

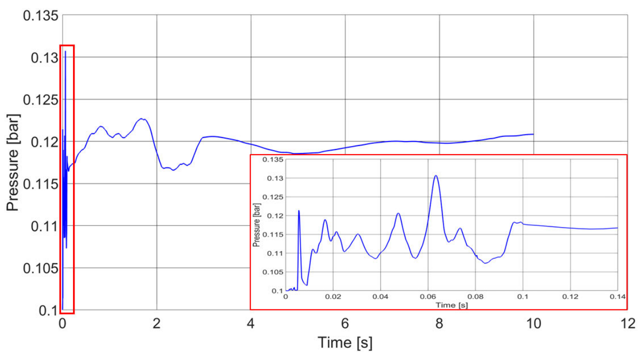

FIGURE 16. Pressure evolution on the probe point located in front of the rupture.

D. SCALING ANALYSIS

To provide a quantitative scaling analysis, the Mach Disk location (L_{MD}) and its diameter (d_{MD}) were compared with the empirical correlations proposed by Hu et al. [31], defined as:

$$L_{MD} = 1.36 \cdot d\sqrt{p_0/p_\infty} \tag{7}$$

$$d_{MD} = 0.65 \cdot d\sqrt{p_0/p_\infty} \tag{8}$$

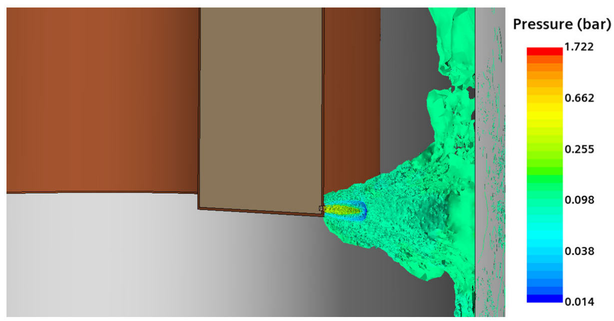

FIGURE 17. Pressure distribution inside the jet core at t = 10.0 s.

TABLE 1. Most important safety-related parameters.

Parameter	Value	Location/Condition
Max Mach Number	2.1	Jet during expansion
Min Temperature	3 K	Expansion zone
Max Pressure	0.13 bar	Wall in front of rupture
Max Heat Flux	$\sim$ 350 W/m^2	CSM internal wall (at t $\sim$ 75 s)
	$\sim$ 550 W/m^2	CSM external wall (at t $\sim$ 75 s)
Avg CSM Temp	6.3 K	At t = 300 s
Avg Cryo Temp	110 K	At t = 300 s

In their work, the authors developed an optimized predictive model to estimate the position and diameter of the Mach disk in underexpanded jets of supercritical fluids, which may undergo phase change and exhibit a specific heat ratio different from that assumed in classical formulations for air or ideal gases. Given a rupture diameter $d = 0.02$ m, a stagnation pressure $p_0 = 6$ bar, and an initial ambient pressure $p_\infty = 0.1$ bar, the theoretical position is $L_{MD} \sim 0.210\,69$ m. The simulation results show the Mach disk stabilizing at $\sim 0.212\,62$ m (see Fig. 18), showing an excellent agreement with the analytical scaling (error < 1%).

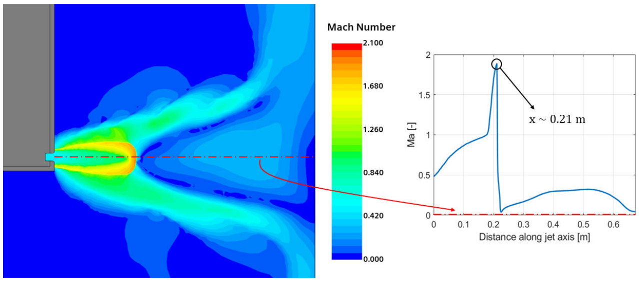

FIGURE 18. Mach number distribution along the jet axis at t = 10.0 s.

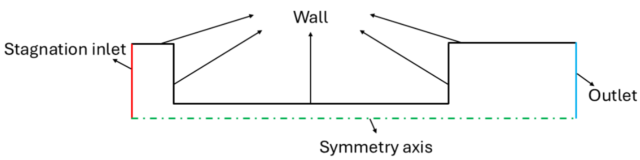

FIGURE 19. Computational domain and boundary conditions of the 2D steady state case.

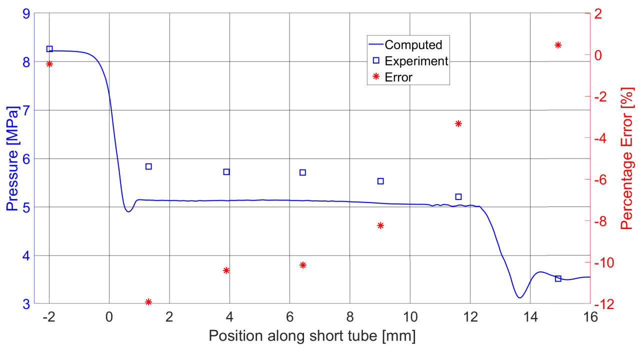

FIGURE 20. Absolute pressure profile along the short tube, for the case with $p_{upstream}$ = 8.23 MPa.

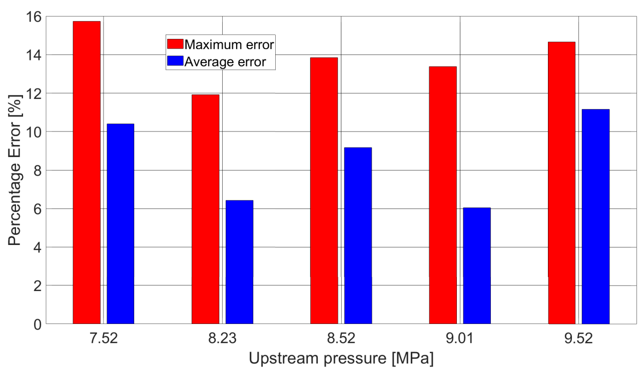

FIGURE 21. Maximum and average error for the five cases.

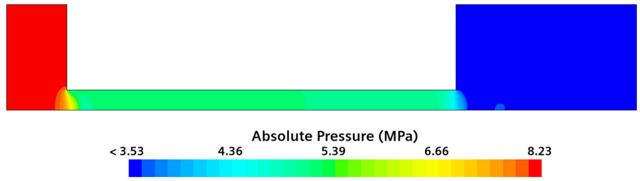

FIGURE 22. Absolute pressure distribution in the domain, for the case with $p_{upstream}$ = 8.23 MPa.

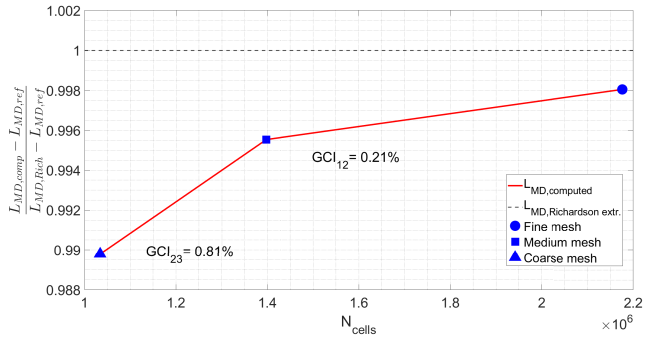

FIGURE 23. GCI analysis on the Mach Disk position L_{MD}.

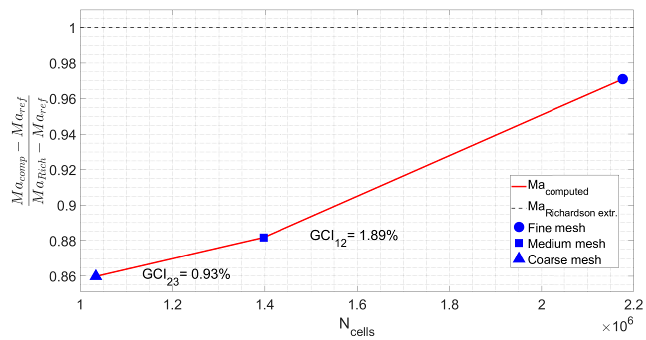

FIGURE 24. GCI analysis on the maximum Mach number Ma_{MAX}.

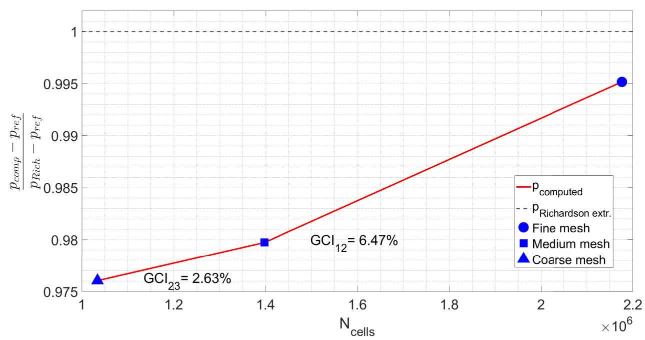

FIGURE 25. GCI analysis on the minimum absolute pressure p_{MIN}

Regarding the disk the diameter, the computed and theoretical values are ~ 0.0915 m and ~ 0.1007 m, respectively (error < 10%). This confirms that the AMR strategy and the 2PTE model, coupled with the SST $k-\omega$ turbulence model are able to accurately capture the fundamental gas dynamics of the expansion. It is worth noting that the use of the classical correlation developed for air, namely:

$$L_{MD} = 0.67 \cdot d\sqrt{p_0/p_\infty} \tag{9}$$

leads to a significant underestimation of the Mach disk location. This discrepancy is physically consistent with the high specific heat ratio of helium ($\gamma = 1.67$) and, more

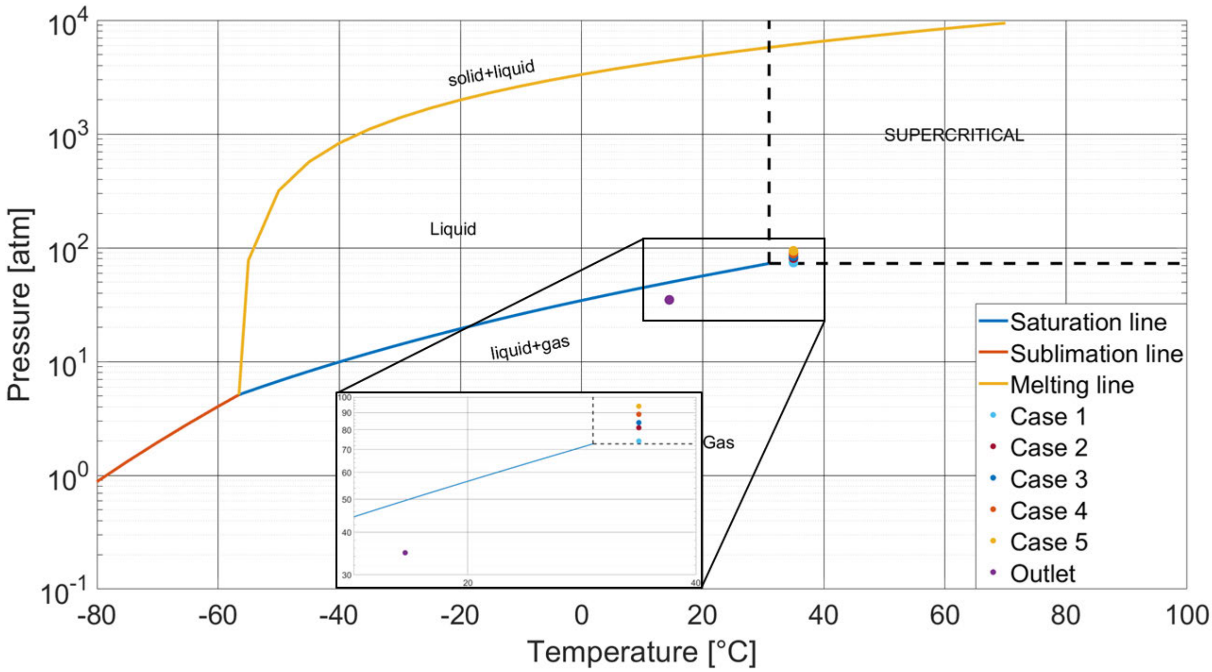

FIGURE 26. CO_2 **state diagram.**

importantly, with the non-ideal gas behavior of supercritical helium near its critical point.

V. CONCLUSION AND PERSPECTIVES

This work presents a comprehensive modeling approach for the thermal-hydraulic analysis of in-cryostat Loss-of-Coolant Accidents (LOCAs) in superconducting magnet systems, with a specific focus on the ITER Central Solenoid Module (CSM). A detailed 3D CFD analysis was performed to capture the transient dynamics of supercritical helium (SHe) discharge and its thermodynamic interaction with the cryostat environment.

The model effectively reproduced the multiphase nature of the underexpanded jet, capturing key flow and thermal features, including shock structures and phase transitions. Additionally, the implementation of Adaptive Mesh Refinement (AMR) proved highly beneficial, ensuring accurate resolution of shock fronts while optimizing computational resources.

Beyond the physical insights, the 3D CFD framework presented here offers a direct contribution to the design and safety assessment of cryogenic facilities. By identifying localized ‘hot spots’ and peak impact zones that are typically averaged out in 0D/1D models, these results can inform the strategic placement of physical deflectors and sensors. This enables earlier detection of transient events and helps mitigate direct jet impingement on sensitive components.

Looking ahead, modeling of the complete cryogenic circuit, including all 40 pancakes and all the LOCA-related components, is currently underway using the 4C code. This ongoing effort will also enable validation of the model against experimental data collected at JT-60SA [32] and at the CSM testing facility in San Diego [9].

Future work will focus on the development of a 3D multiphysics model of the electric arc responsible for damaging the terminal joints, with the ultimate goal of reconstructing the full sequence of events leading to the LOCA transient and further enhancing the predictive capabilities of accident simulations.

APPENDIX A
MULTIPHASE MODEL VALIDATION

The multiphase model described in Section III-C1 is validated here against published experimental data [33]. In the absence of dedicated experimental data for supercritical helium expansion into vacuum, the multiphase model is validated here against published experimental data for supercritical CO_2. This choice aims to verify the capability of the 2PTE model to accurately capture phase-change dynamics in supercritical fluids, regardless of the specific medium, thus only a subset of the configurations proposed in [33] is examined. In particular, the case where the upstream pressure is varied to observe the effects on the mass flow rate, is analyzed and compared with the published results. Even though the present case is fully 3D and transient, this 2D steady state model should allow testing the most suitable configuration to be later implemented in the 3D analysis, except for the AMR solver, which can only be applied in three-dimensional simulations.

A. SETUP

The computational domain is shown in Fig. 19, together with the boundary conditions, listed below:

- Inlet: stagnation inlet with fixed supersonic pressure, total pressure, and total temperature
- Outlet: pressure outlet with fixed pressure and temperature (3.53 MPa, 287.6 K)
- Bottom boundary: symmetry axis
- Walls: no slip condition

The inlet pressure is varied across five distinct cases, from 7.52 MPa to 9.52 MPa, while the inlet temperature is kept constant at 308.15 K.

B. MODEL

The adopted models are analogous to those used in the 3D simulation, with some exception (2D/3D, steady/transient). The models are briefly listed below:

a) 2D axisymmetric
b) Steady
c) Turbulent (SST $k-\omega$ [22], [23], [24], [25], [26])
d) Multiphase
e) Two-Phase Thermodynamic Equilibrium (2PTE)
f) Coupled flow
g) Coupled energy

C. RESULTS

The simulation results are compared against the experimental data reported by Liu et al. [33]. Fig. 20 shows the absolute pressure profile along the pipe, together with the percentage error between the computed and the reference values for the case with $p_{upstream} = 8.23$ MPa. To provide a complete overview of all five configurations, the maximum and average errors for each case are summarized in Fig. 21. The absolute pressure distribution in the whole domain is also shown in Fig. 22. The numerical results demonstrate good agreement with the experimental data reported in [33]. In particular, the computed pressure profiles closely follow the experimental data points, with average errors of approximately 10% or less for all the analyzed cases. These findings confirm that the adopted multiphase model is reliable and suitable for application to the 3D transient simulation. For clarity, the five inlet conditions used in the simulations, together with the common outlet condition, are shown on the CO_2 state diagram in Fig. 26.

APPENDIX B
GRID INDEPENDENCE ANALYSIS

A mesh sensitivity study was performed to evaluate the impact of the discretization level on the accuracy of the supersonic jet evolution. The analysis follows the procedure described by Schwer in [34], which is based on the well-established Grid Convergence Index (GCI) methodology originally proposed by Roache [35], [36], [37]. Three different mesh configurations (Coarse, Medium, and Fine) were compared, focusing on the target minimum cell size δ_{min}. The values tested for δ_{min} were 1.6 mm, 1.2 mm, and 0.8 mm, respectively. The convergence was assessed by monitoring three primary parameters along the jet axis during the first 4 ms of the transient: the maximum Mach number (Ma_{MAX}), the minimum absolute pressure (p_{MIN}), and the axial position of the Mach disk (L_{MD}). The results of the GCI analyses are presented in Figs. 23, 24, 25. The results confirm that the 0.8 mm threshold provides a robust discretization for the shock fronts. Further refinement leads to a significant increase in computational cost without a corresponding gain in physical accuracy. Therefore, the AMR settings used in this work are considered optimized for capturing the complex 3D dynamics of the supercritical helium jet while maintaining a feasible computational timeframe for the long-term thermal analysis.

ACKNOWLEDGMENT

The Views and opinions expressed are, however, those of the author(s) only and do not necessarily reflect those of European Union or European Commission. Neither European Union nor European Commission can be held responsible for them.

REFERENCES

[1] A. Retheesh, F. A. Hernández, and G. Zhou, "Application of inelastic method and its comparison with elastic method for the assessment of in-box LOCA event on EU DEMO HCPB breeding blanket cap region," *Appl. Sci.*, vol. 11, no. 19, p. 9104, Sep. 2021.

[2] F. Galleni, M. Moscardini, M. Eboli, A. Del Nevo, D. Martelli, and N. Forgione, "Preliminary analysis of an in-box LOCA in the breeding unit of the WCLL TBM for the ITER reactor with SIMMER-IV code," *Fusion Eng. Design*, vol. 169, Aug. 2021, Art. no. 112472.

[3] A. Zappatore, A. Froio, G. A. Spagnuolo, and R. Zanino, "3D transient CFD simulation of an in-vessel loss-of-coolant accident in the EU DEMO fusion reactor," *Nucl. Fusion*, vol. 60, no. 12, Aug. 2020, Art. no. 126001.

[4] M. Spro, A. Froio, and A. Zappatore, "3D transient CFD simulation of an in-vessel loss-of-coolant accident in the EU DEMO WCLL breeding blanket," *Energies*, vol. 16, no. 9, p. 3637, Apr. 2023.

[5] N. Martovetsky et al., "Testing of the ITER central solenoid modules," *IEEE Trans. Plasma Sci.*, vol. 50, no. 11, pp. 4292–4297, Nov. 2022.

[6] J. Huang, J. Wei, J. Ge, S. Liu, Y. Song, and T. Jin, "Numerical investigation of a highly underexpanded jet with real gas effects during the loss of coolant accident in a cryostat: Flow and heat transfer characteristics," *Appl. Thermal Eng.*, vol. 268, Jun. 2025, Art. no. 125861.

[7] M. Draksler, B. Končar, M. Tekavčič, and C. Bachmann, "CFD analysis of the natural circulation of helium in the DEMO cryostat during a leak accident," *Fusion Eng. Design*, vol. 158, Sep. 2020, Art. no. 111752.

[8] K. Nishida, T. Honda, K. Hamada, K. Matsui, T. Kato, H. Tsuji, N. Mitchell, and K. Yoshida, "The pressure rise simulation when helium pipes are broken in the ITER cryostat," in *Advances in Cryogenic Engineering*, vol. 43. New York, NY, USA: Springer, 1998, pp. 361–368.

[9] K. Khumthong, E. Ortiz, J. Sheeron, B. Fledderman, N. Norausky, J. Smith, S. Patlan, N. Martovetsky, K. Freudenberg, G. Rossano, K. Wooley, T. Schild, N. Mitchell, Y. Miyoshi, and A. Langhorn, "ITER CS module test facility operational lessons from CS modules 1–4," *IEEE Trans. Appl. Supercond.*, vol. 34, no. 5, pp. 1–6, Aug. 2024.

[10] General Atomics. (2021). *General Atomics Completes Fabrication and Testing of First ITER Central Solenoid Module*.[Online]. Available: https://www.ga.com/general-atomics-completes-fabrication-and-testing-of-first-iter-central-solenoid-module

[11] G. Rolando, A. Devred, and A. Nijhuis, "Temperature and current margin of ITER central solenoid conductor designs during a 15 MA plasma scenario," *Superconductor Sci. Technol.*, vol. 27, no. 2, Feb. 2014, Art. no. 025010.

[12] J. Schultz, T. A. Antaya, J. Feng, C. Gung, N. Martovetsky, J. V. Minervini, P. C. Michael, A. Radovinsky, and P. Titus, "The ITER central solenoid," in *Proc. 21st IEEE/NPS Symp. Fusion Eng.*, Aug. 2005, pp. 1–4.

[13] Siemens Digital Industries Software. (2021). *Simcenter STAR-CCM+*. [Online]. Available: https://plm.sw.siemens.com/it-IT/simcenter/fluids-thermal-simulation/star-ccm/

[14] I. H. Bell, J. Wronski, S. Quoilin, and V. Lemort, "Pure and pseudo-pure fluid thermophysical property evaluation and the open-source thermophysical property library CoolProp," *Ind. Eng. Chem. Res.*, vol. 53, no. 6, pp. 2498–2508, Feb. 2014.

[15] V. J. Johnson, "A compendium of the properties of materials at low temperature (Phase I), Part II: Properties of solids," National Bureau of Standards, New Delhi, India, Tech. Rep. 60-56, 1961.

[16] G.Hartwig, "Low temperature properties of resins and their correlations," *Adv. Cryog. Eng.*, vol. 24, 1978.

[17] N. J. Simon, E. S. Drexler, and R. P. Reed, "Properties of copper and copper alloys at cryogenic temperatures, volume 177 of NIST monograph," National Institute of Standards and Technology, Gaithersburg, MD, USA, Tech. Rep., 1992.

[18] X. Wei, X. Hao, A. Bergara, E. Zurek, X. Liang, L. Wang, X. Song, P. Li, L. Wang, G. Gao, and Y. Tian, "Designing ternary superconducting hydrides with A15-type structure at moderate pressures," *Mater. Today Phys.*, vol. 34, May 2023, Art. no. 101086.

[19] J. Lu, R. P. Walsh, and K. Han, "Low temperature physical properties of a high mn austenitic steel JK2LB," *Cryogenics*, vol. 49, nos. 3–4, pp. 133–137, Mar. 2009.

[20] *Simcenter STAR-CCM+ User Guide V. 2021.2*, Siemens Digital Industries Software, Plano, TX, USA, 2021.

[21] M. De Lorenzo, P. Lafon, M. D. Matteo, M. Pelanti, J.-M. Seynhaeve, and Y. Bartosiewicz, "Homogeneous two-phase flow models and accurate steam-water table look-up method for fast transient simulations," *Int. J. Multiphase Flow*, vol. 95, pp. 199–219, Oct. 2017.

[22] F. R. Menter, "Two-equation eddy-viscosity turbulence models for engineering applications," *AIAA J.*, vol. 32, no. 8, pp. 1598–1605, Aug. 1994.

[23] N. Georgiadis, D. Yoder, and W. Engblom, "Evaluation of modified two-equation turbulence models for jet flow predictions," in *Proc. 44th AIAA Aerosp. Sci. Meeting Exhib.*, Jan. 2006, pp. 1–16.

[24] C. L. Rumsey, "Exploring a method for improving turbulent separated-flow predictions with k-ω models," NASA Langley Research Center, Hampton, Virginia, Tech. Rep. NASA/TM-2009-215952, 2009.

[25] J. E. Bardina, P. G. Huang, and T. J. Coakley, "Turbulence modeling validation, testing, and development," National Aeronautics and Space Administration, Moffett Field, CA, USA, Tech. Rep., Apr. 110446, 1997.

[26] D. A. Yoder, "Assessment of turbulence models for a single-injector cooling flow," in *Proc. AIAA SCITECH Forum*, Jan. 2022, p. 620.

[27] A. Moscatello, A. C. Uggenti, R. Gerboni, and A. Carpignano, "A novel approach to high-pressure gas releases simulations," *J. Loss Prevention Process Industries*, vol. 72, Sep. 2021, Art. no. 104531.

[28] A. H. Shapiro, *The Dynamics and Thermodynamics of Compressible Fluid Flow*, vol. 1. New York, NY, USA: Wiley, 1953.

[29] J. D. Anderson, *Modern Compressible Flow With Historical Perspective*, 3rd ed., New York, NY, USA: McGraw-Hill, 2003.

[30] L. Savoldi Richard, F. Casella, B. Fiori, and R. Zanino, "The 4C code for the cryogenic circuit conductor and coil modeling in ITER," *Cryogenics*, vol. 50, no. 3, pp. 167–176, Mar. 2010.

[31] Y. Hu, L. Chen, Z. Cao, K. Yang, X. Yan, and J. Yu, "Experimental study on supercritical CO_2 jet characteristics and coal breakage utilization in carbon capture, utilization and storage (CCUS) process," *Process Saf. Environ. Protection*, vol. 184, pp. 260–270, Apr. 2024.

[32] H. Shirai, K. Takahashi, and E. D. Pietro, "Recent progress of JT-60SA project toward plasma operation," *Nucl. Fusion*, vol. 64, no. 11, 2024, Art. no. 112008.

[33] J. P. Liu, Y. M. Niu, J. P. Chen, Z. J. Chen, and X. Feng, "Experimentation and correlation of R744 two-phase flow through short tubes," *Experim. Thermal Fluid Sci.*, vol. 28, no. 6, pp. 565–573, Jun. 2004.

[34] L. E. Schwer, "Is your mesh refined enough? Estimating discretization error using GCI," Schwer Engineering & Consulting Services, Bamberg, Germany, Tech. Rep., 2008.

[35] Patrick J. Roache, "A method for uniform reporting of grid refinement studies," in *Proceedings of Quantification of Uncertainty in Computation Fluid Dynamics*, I. Celik, Ed., Washington, DC, USA: ASME Publ., 1993, pp. 230–240.

[36] P. J. Roache, "Perspective: A method for uniform reporting of grid refinement studies," *J. Fluids Eng.*, vol. 116, no. 3, pp. 405–413, Sep. 1994.

[37] P. J. Roache, *Verification and Validation in Computational Science and Engineering*. Albuquerque, NM, USA: Hermosa Publishers, 1998.

MAURO SPRÓ was born in Maglie, Italy, in 1998. He received the B.Sc. degree in energy engineering and the M.Sc. degree in energy and nuclear engineering from the Politecnico di Torino, Turin, Italy, in 2021 and 2023, respectively. He is currently pursuing the Ph.D. degree in energy engineering.

His research interests include the detailed modeling of nuclear fusion reactors components to perform safety-related analyses as well as system-level thermal–hydraulic analyses on the cooling loops for the cryogenic plant of tokamaks.

ANTONIO FROIO received the B.Sc. degree in mechanical engineering from Universitá della Calabria, Rende, Cosenza, Italy, in 2012, the M.Sc. degree in energy and nuclear engineering from the Politecnico di Torino (PoliTo), Turin, Italy, in 2014, the double M.Sc. degree in nuclear engineering from the Politecnico di Milano, Milan, Italy, in 2015, the joint Alta Scuola Politecnica Diploma degree from the PoliTo and the Politecnico di Milano, in 2015, and the Ph.D. degree in energetics from the PoliTo, in 2018.

From 2018 to 2021, he was a Research Fellow with the Energy Department, Politecnico di Torino, where he was an Assistant Professor, from 2022 to 2025, and has been an Associate Professor, since 2025. He has authored or co-authored more than 40 articles in international journals concerning the development and application of system-level models for tokamak fusion reactors, the CFD analysis of different fusion components, and multi-physics modeling of the breeding blanket. He is involved in the design of the EU DEMO in-vessel components and related auxiliary systems. He is a co-inventor of two patents.

Prof. Froio is a member of American Nuclear Society and the Associazione Italiana Nucleare. He was awarded the EUROfusion Engineering Grant, in 2018.

ANDREA ZAPPATORE received the M.Sc. degree in energy and nuclear engineering and the Ph.D. degree in energetics from the Politecnico di Torino (PoliTo), Turin, Italy, in 2016 and 2021, respectively.

He is currently an Assistant Professor with PoliTo. He has co-authored 35 articles published in international journals, focused on computational modeling in nuclear fusion systems and components. His research interests include the development, verification, validation, and application of new modeling tools for both low and high temperature superconducting magnets, and the computational fluid dynamics modeling of high heat flux components and accidental scenarios. He received the EUROfusion Researcher Grant for the development and validation of quench and AC loss models for high temperature superconducting cable-in-conduit conductors for the EU-DEMO central solenoid.